

TURBULENCE STRUCTURES IN AN AXISYMMETRIC ADVERSE-PRESSURE-GRADIENT BOUNDARY LAYER AND THEIR ROTOR AEROACOUSTIC RESPONSE

Di Zhou, Kan Wang and Meng Wang

Department of Aerospace and Mechanical Engineering
University of Notre Dame
Notre Dame, IN 46556, USA
dzhou@nd.edu, kwang2@nd.edu, m.wang@nd.edu

ABSTRACT

The flow over an axisymmetric body of revolution (BOR) is investigated numerically at Reynolds number of 1.9×10^6 based on the BOR length, with a focus on the decelerating turbulent boundary layer in the tail-cone section and its acoustic radiation when ingested by a rotor. The boundary layer on the nose and midsection of the BOR is computed using wall-modeled LES whereas that in the acoustically important tail-cone section is wall resolved. The radiated acoustic field is calculated based on the Ffowcs Williams-Hawkings equation. The computed flow statistics and sound pressure spectra agree well with the experimental measurements at Virginia Tech. Correlation and spectral analyses demonstrate rapidly growing turbulence structures in the tail-cone boundary layer, whose interaction with successive rotor blades generates coherent unsteady-loading dipole sources on neighboring blades and thereby haystacking peaks in the broadband sound pressure spectra. The spatial and frequency characteristics of blade acoustic dipole sources and their correlations are examined.

INTRODUCTION

The noise produced by a rotor ingesting a turbulent boundary layer (TBL) and/or wake is of considerable interest in many aeronautical, marine, automotive and wind-energy applications. The noise level and spectral characteristics are strongly dependent on the turbulent inflow, which is in general spatially inhomogeneous and often subjected to complex pressure-gradient and surface-curvature effects. Accurate prediction and modeling of rotor turbulence-ingestion noise require knowledge of not only low-order statistics but also structures of the inflow turbulence.

This study is aimed at numerically predicting the noise of rotor interaction with a thick turbulent boundary layer at the rear of an axisymmetric body of revolution (BOR) and elucidating the acoustic source mechanisms. The BOR is at zero angle of attack and thus the TBL is also axisymmetric statistically. Of particular interest is the generation of spectral humps, known as haystacking peaks, in the broadband sound pressure spectra near the blade passing frequency (BPF) and its harmonics, and their relation to the turbulence structures in the boundary layer. The BOR-rotor configuration is of practical significance as it captures the key physics of rotor interaction with fuselage (hull) boundary layers on flight (marine) vehicles.

Researcher at Virginia Tech (VT) recently conducted experiments to study the sound from a five-bladed rotor ingest-

ing the axisymmetric TBL of a BOR (Hickling et al., 2019; Hickling, 2020; Balantrapu et al., 2021). The evolution of the tail-cone boundary layer was examined through measurements of single-point velocity statistics and two-point velocity correlations at the rotor inlet plane, and their unsteady pressure footprint on the tail-cone surface was also measured. Acoustic measurements, conducted at different rotor advance ratios, showed broadband noise and haystacking peaks at frequencies 7–12% higher than the BPF and its harmonics. In the present work, the BOR boundary layer and its interaction with the rotor as in the VT experiment are simulated numerically, and the results are validated by the experimental data. To gain a detailed understanding of the acoustic source mechanisms, a systematic analysis is conducted on the evolution of velocity two-point and spatiotemporal correlations in the tail-cone TBL, acoustic dipole source distributions on rotor blades, and blade-to-blade correlations and coherence of the dipole sources.

COMPUTATIONAL APPROACH

The BOR geometry, shown in figure 1a, consists of a cylindrical midsection of diameter D and equal length, an ellipsoidal nose of length D , and a tail cone with a 20° half apex-angle that is connected to a thin cylindrical support pole of diameter $0.15D$. The tail-cone angle was selected to achieve the thickest possible boundary layer at the tail end without flow separation. The Reynolds number based on the free-stream velocity U_∞ and the length of the body, $L = 3.17D$, is 1.9×10^6 . Transition to turbulence is triggered by a circumferential trip ring located at the end of the nose. Large-eddy simulation (LES) is conducted under the VT experimental conditions with and without a five-bladed rotor installed at the tail-cone end of the BOR. The rotor, whose geometry is shown in figure 1b, has a diameter of $0.5D$ and is at the advance ratio of $J = 1.44$, which nominally corresponds to zero thrust.

A finite volume, unstructured-mesh LES code for incompressible flow developed at Stanford University (You et al., 2008) was adapted and enhanced to carry out the flow simulations. It employs energy-conserving and low-dissipative spatial discretization, a fully implicit fractional-step method for time advancement, the Generalized Product Bi-Conjugate Gradient with safety convergence (GPBiCGSafe) method for the pressure Poisson equation, and the dynamic subgrid-scale model. The BOR-rotor flow is simulated in the rotor frame of reference using the absolute velocity formulation. To reduce the computational cost, wall modeling is employed in the nose and midsection regions of the BOR while the acoustically im-

portant tail-cone section is wall-resolved.

Simulations are conducted in a cylindrical domain with the same blockage ratio as in the VT wind tunnel. It is $11.2D$ long and $2.39D$ in radius. Structured-mesh blocks are used around the entire BOR, rotor blades, the rotor hub and the support pole, and unstructured mesh blocks are employed elsewhere. Approximately 5×10^8 mesh cells are used for the BOR block. The wall-resolved tail-cone section has 1200 streamwise cells and 1600 azimuthal cells, both uniformly spaced, and 130 cells across the thickness of the boundary layer at the end of the cone. Grid convergence for flow over the BOR has been established through simulations without the rotor on coarser and finer meshes (Zhou et al., 2020). In the rotor block, two meshes with 5×10^7 and 1.2×10^8 cells are employed to evaluate the grid convergence of the rotor acoustic response.

Noise calculations are based on the Ffowcs Williams-Hawkings (FW-H) equation (Ffowcs Williams and Hawkings, 1969). At low Mach numbers sound generation is dominated by the unsteady forces on rotor blades, and the sound pressure at an acoustic far-field location \mathbf{x} and time t can be computed from (Brentner and Farassat, 2003; Wang et al., 2021)

$$p(\mathbf{x}, t) \approx \frac{1}{4\pi c_\infty} \frac{\partial}{\partial t} \int_S \left[\frac{r_{di}}{r_d^2} \frac{p_{ij} n_j}{|1 - M_r|} \right]_{\tau^*} dS \quad (1)$$

where c_∞ is the free-stream speed of sound, p_{ij} is the compressive stress tensor dominated by pressure, n_j are components of the unit normal vector of the blade surface S pointing into the fluid, $r_d = |\mathbf{x} - \mathbf{y}(\tau)|$ is the distance between the observer and the source coordinates, $r_{di} = x_i - y_i$, and $M_r = (r_{di}/r_d)M_i$ is the Mach number of the source in the radiation direction with M_i being components of the source Mach number vector. The integrand is evaluated at the retarded time τ^* , which is the root of the equation $\tau = t - |\mathbf{x} - \mathbf{y}(\tau)|/c_\infty$. Acoustic scattering by the BOR, significant only at high frequencies and shallow observer angles relative to the flow direction, is ignored in the calculation. Accuracy of this computational approach has been demonstrated by Wang et al. (2021) for rotor noise generation in a turbulent wake by comparison with experimental results.

TAIL-CONE BOUNDARY LAYER

Figure 1a shows an instantaneous flow field in terms of isocontours of the axial velocity in a plane through the BOR axis. The flow accelerates around the nose and on approach to the sharp corner between the midsection and the tail cone. Downstream of the corner, the flow decelerates under the influence of strong adverse pressure gradient (APG), and the boundary layer thickens rapidly. A comparison of the computed velocity statistics with the PIV measurements at VT (Hickling, 2020; Balantrapu, 2021) is shown in figure 2 for $x/D = 2.17$, which is at the end of the BOR tail-cone. This location is only $0.055D$ upstream of the rotor leading edge and thus considered the rotor inlet plane in the following analysis. The agreement between the LES and experimental profiles is reasonable for both the mean axial velocity and the root-mean-square (r.m.s.) values of axial and azimuthal velocity fluctuations. Although there are small discrepancies in the velocity fluctuations, the overall distributions and locations of peak fluctuations agree well with the experiment. More extensive validation against experimental measurements has been conducted for BOR flow without a rotor under otherwise the same conditions (Zhou et al., 2020), and good agreements have been obtained for velocity statistics and energy spectra at various

axial locations as well as the magnitude and frequency spectra of pressure fluctuations on the tail-cone surface.

The evolution of turbulence structures in the tail-cone TBL is investigated through spectral and correlation analyses. Figure 3 depicts the two-point correlations of the fluctuating axial velocity in a center plane through the BOR axis for seven anchor positions. These anchor points are along a mean streamline that passes through $(x/D, r/D) = (2.17, 0.18)$, which is in the vicinity of peak turbulence intensity in the rotor inlet plane. It can be seen that the spatial scales of flow structures increase rapidly in the downstream direction with growing TBL thickness. The corresponding correlations from the LES without a rotor (not shown) are virtually the same except at the last station, where the effect of the rotor becomes noticeable. The two-point correlations of the fluctuating pressure on the tail-cone surface have also been examined, and they exhibit even more drastic increases in length scales in the downstream direction (Zhou et al., 2020). Two-point correlations of the fluctuating axial velocity in the y - z plane at the tail-cone end with and without the rotor are compared in figure 4. The correlation lengths in both radial and azimuthal directions are increased by the rotor, although the growth of the azimuthal correlation length is small. Two negative correlation regions are observed when the rotor is present.

Figure 5 shows the radial spatial-temporal correlations of the fluctuating axial velocity at the tail-cone end with the anchor position at $(x/D, r/D) = (2.17, 0.18)$. Results from simulations with and without the rotor are both illustrated. The correlation contours for the flow undisturbed by a rotor show a typical convective pattern with a small negative convection velocity in the radial direction. In the presence of the rotor, multiple strips of relatively low-correlation levels appear due to fluid motions induced by the rotating blades. The main correlation contours are distorted and show interaction of coherent structure with successive blades. As will be discussed in the next section, such interaction leads to blade-to-blade correlations and coherence between the unsteady-loading dipole sources, and thereby gives rise to haystacking in the sound pressure spectra.

ACOUSTICS AND SOURCE ANALYSIS

Figure 6 shows the sound pressure levels (SPLs) predicted numerically using equation (1) with surface pressure obtained from the LES along with the integrated spectra measured by Hickling et al. (2019) with a 64-channel microphone array. The free-stream Mach number is 0.059, and the center of the microphone array is at a distance of $3.86D$ from the rotor center and 106° counter-clockwise from the downstream direction. The computed spectra are obtained by averaging the spectra from all 64 microphone positions in the array. Two sets of LES data, from the coarse and fine meshes in the rotor block, are presented. The SPLs are in dB per Hz with reference to 2×10^{-5} Pa, and the frequency is normalized by the BPF.

It can be observed that the sound pressure spectra are broadband with four distinct haystacking peaks. These peaks occur at frequencies 8–12% higher than (i.e., right-shifted) the BPF and its first three harmonics. The numerical predictions from the two meshes compare well for frequencies up to ten times the BPF, demonstrating grid convergence. They are also in reasonable agreement with the experimental spectrum over the frequency range of the experimental data. In particular, the simulations capture the haystacking peaks and their frequencies, although the peak levels are underpredicted by 2–

4 dB. The broadband component of the sound is predicted accurately.

To reveal the acoustic source characteristics and the mechanisms for generating the haystacking phenomenon, it is illuminating to examine the unsteady sectional force, $f_i = \int p_{ij} n_j d\Gamma$ where Γ is along the blade circumference at given radial position r , and its time derivative $\partial f_i / \partial t$. The latter is representative of the sectional acoustic dipoles associated with rotor blades. If the blade chord is acoustically compact, which is the case at low and intermediate frequency, equation (1) can be rewritten as

$$p(\mathbf{x}, t) \approx \frac{1}{4\pi c_\infty} \frac{\partial}{\partial t} \sum_{n=1}^{N_b} \int_{R_{\text{hub}}}^{R_{\text{tip}}} \left[\frac{r_{d_i}}{r_d^2} \frac{f_i}{|1 - M_r|} \right]^n dr \quad (2)$$

where N_b is the number of blades, and R_{hub} and R_{tip} are the radii of the blade hub and tip, respectively. Sectional force and dipole properties are particularly useful for theoretical modeling of rotor noise (e.g., Glegg et al., 2015).

Figure 7 shows the radial distributions of the frequency spectra of the unsteady sectional force and dipole source at five discrete frequencies corresponding to the four haystacking peaks and a higher frequency. Only the component perpendicular to the chord, denoted by L , is considered since it is significantly larger in magnitude than the chordwise component. The level of the sectional-force spectra decreases with increasing frequency and grows in the radial direction initially until the blade outer region. The location of the spectral peak depends on the frequency, but in terms of the overall magnitude, i.e., the r.m.s. of L , the maximum value is reached at $r/D \approx 0.18$, which coincides with the location of the maximum chord length and turbulence intensity. For the spectra of the sectional dipole, $D_L = \partial L / \partial t$, the radial variations are similar to those of the sectional-force spectra but their frequency variations are much weaker and non-monotonic. Among the five frequencies, the second haystacking peak at $f/f_{BP} \approx 2.2$ has the highest dipole spectral level overall. It should be mentioned that the weak oscillations in the spectral curves seen in the figure are caused by limited statistical sampling period, and they do not affect the above conclusions.

Figure 8 shows the correlations of the unsteady sectional forces, $C_{LL}^{(m,n)}(r, \Delta r, \Delta t)$, between one blade (blade m) at the location of maximum chord length, $r/D = 0.18$, and those on several blades (blade n) including itself at varying radial positions. Correlations are strong with the neighboring blade at the front (figure 8a), the same blade (figure 8b), and the neighboring blade at the back (figure 8c). Correlations with the second neighboring blade at the back (figure 8d) are significantly weaker. The location of maximum correlation moves downward from above the anchor point on the front neighbor to the anchor point on the same blade, and then to below the anchor point on the back neighbor. This downward shift is related to the downward convection of the coherent turbulence structures in the tail-cone boundary layer, as can be seen in the two-point velocity correlations in figure 3. Blade-to-blade correlations of the sectional forces are caused by successive blades interacting with the same coherent structure (cf. figure 5a). As the structure is convected downstream and through the rotor, succeeding blades cut through the same structure at lower positions, leading to the downward shift of the maximum correlation location on the blades. It can be noticed that the temporal separations corresponding to maximum correlations are slightly less than the corresponding blade-passage times. This is related to the right-shift of haystacking frequencies due to the diagonal track taken by the rotating blades through the convecting turbulence structures (Murray et al., 2018; Martinez, 1996). The

blade-to-blade correlations of the sectional dipole sources (not shown) exhibit the same trend as the sectional forces but the correlation levels are lower since the time derivative places more weights on smaller scales (Wang et al., 2021). Nonetheless, they are sufficient to generate haystacking in the radiated sound pressure spectra.

The statistical dependence among blades in the frequency domain can be determined by examining the coherence of blade sectional dipole sources, which is the same as the coherence of sectional forces for stationary turbulence (Yang and Wang, 2013). Figure 9 shows the coherence between the sectional dipole source at $r/D = 0.18$ on a blade and those on a front neighbor, itself, and two back neighbors at varying radial positions. On the same blade (figures 9b), the coherence length decreases with frequency and becomes very small at high frequencies. Regions of pronounced coherence are found on the two neighboring blades in the forward (figure 9a) and backward (figure 9c) directions around the frequencies of haystacking peaks and valleys between these peaks in the sound pressure spectra (cf. figure 6). As the frequency increases, the coherence decays gradually and becomes insignificant beyond 3.5 times the BPF. The value of the coherence with the second neighboring blade at the back (figure 9d) is smaller than 0.2 at low frequencies and practically negligible at higher frequencies. As in the correlation figure, the region of large coherence shifts downward on succeeding blades as a result of the downward convection of the turbulence structures. The significant source coherence between neighboring blades leads to strong interference among radiated acoustic waves at these discrete frequencies. At the haystacking frequencies, the interference is constructive, resulting in the peaks in the rotor sound pressure spectra. At the frequencies between two neighboring haystacking peaks, destructive interference causes the valleys in the spectra. Additionally, figure 9 indicates that the same coherent structure is cut through by only two successive blades, which is consistent with figure 5a and apparently sufficient to generate the haystacking effect.

CONCLUSIONS

The development of an axisymmetric turbulent boundary layer in the tail-cone section of a BOR and its interaction with a five-bladed rotor have been investigated numerically to predict the rotor turbulence-ingestion noise and elucidate the noise source mechanisms. The results presented in this paper demonstrate accurate prediction of the boundary-layer turbulence structures by LES and, in conjunction with the FW-H equation, accurate prediction of the radiated acoustic field under experimental conditions. The two-point correlations of velocity fluctuations show significant growth of turbulence length scales in the downstream direction under strong APG. The computed sound pressure spectra are broadband with haystacks caused by successive blades cutting through the same turbulence structure. Acoustic sources are analyzed in terms of the blade sectional unsteady-loading dipole, whose strength increases with the local chord length, inflow turbulence intensity and rotational speed, and is largest in the outer region near the location of maximum chord length. As anticipated from the velocity two-point and space-time correlations, large correlations are found between sectional dipole sources on neighboring blades, and the corresponding blade-to-blade coherence is significant around the frequencies of haystacking peaks and valleys. The acoustic interference among correlated blade dipoles gives rise to the haystacks in the rotor noise spectra.

ACKNOWLEDGEMENTS

This work was supported by the U.S. Office of Naval Research under Grants N00014-17-1-2493 and N00014-20-1-2688, with Drs. Ki-Han Kim and Yin Lu Young as Program Officers. Computer time was provided by the U.S. Department of Defense High Performance Computing Modernization Program. The authors acknowledge Drs. William Devenport, Nathan Alexander, N. Agastya Balantrapu and Christopher Hickling for providing experimental data.

REFERENCES

Balantrapu, N. A. 2021 The space-time structure of an axisymmetric turbulent boundary layer ingested by a rotor. PhD Thesis, Virginia Tech, Blacksburg, VA.
Balantrapu, N. A., Hickling, C., Alexander, W. N. & Devenport, W. 2021 The structure of a highly decelerated axisymmetric turbulent boundary layer. *Journal of Fluid Mechanics* **929**, A9.
Brentner, K. S. & Farassat, F. 2003 Modeling aerodynamically generated sound of helicopter rotors. *Progress in Aerospace Sciences* **39**, 83–120.
Ffowcs Williams, J. & Hawkins, D. 1969 Sound generation by turbulence and surfaces in arbitrary motion. *Philosophical Transactions of the Royal Society* **264**, 321–342.
Glegg, S. A. L., Devenport, W. J. & Alexander, W. N. 2015 Broadband rotor noise predictions using a time domain approach. *Journal of Sound and Vibration* **335**, 115–124.

Hickling, C. 2020 Inhomogeneous, anisotropic turbulence ingestion noise in two open rotor configurations. PhD Thesis, Virginia Tech, Blacksburg, VA.

Hickling, C., Balantrapu, N. A., Alexander, W. N. A., Millican, J., Devenport, W. J. & Glegg, S. A. 2019 Turbulence ingestion into a rotor at the rear of an axisymmetric body. *AIAA Paper 2019-2571, 25th AIAA/CEAS Aeroacoustics Conference*, 20–23 May, 2019, Delft, The Netherlands.

Martinez, R. 1996 Asymptotic theory of broadband rotor thrust, Part II: Analysis of the right frequency shift of the maximum response. *Journal of Applied Mechanics* **63**, 143–148.

Murray, H. H., Devenport, W. J., Alexander, W. N., Glegg, S. A. L. & Wisda, D. 2018 Aeroacoustics of a rotor ingesting a planar boundary layer at high thrust. *Journal of Fluid Mechanics* **850**, 212–245.

Wang, J., Wang, K. & Wang, M. 2021 Computational prediction and analysis of rotor noise generation in a turbulent wake. *Journal of Fluid Mechanics* **908**, A19.

Yang, Q. & Wang, M. 2013 Boundary-layer noise induced by arrays of roughness elements. *Journal of Fluid Mechanics* **727**, 282–317.

You, D., Ham, F. & Moin, P. 2008 Discrete conservation principles in large-eddy simulation with application to separation control over an airfoil. *Physics of Fluids* **20**, 101515.

Zhou, D., Wang, K. & Wang, M. 2020 Large-eddy simulation of an axisymmetric boundary layer on a body of revolution. *AIAA Paper 2020-2989, AIAA Aviation Forum*, 15–19 June, 2020.

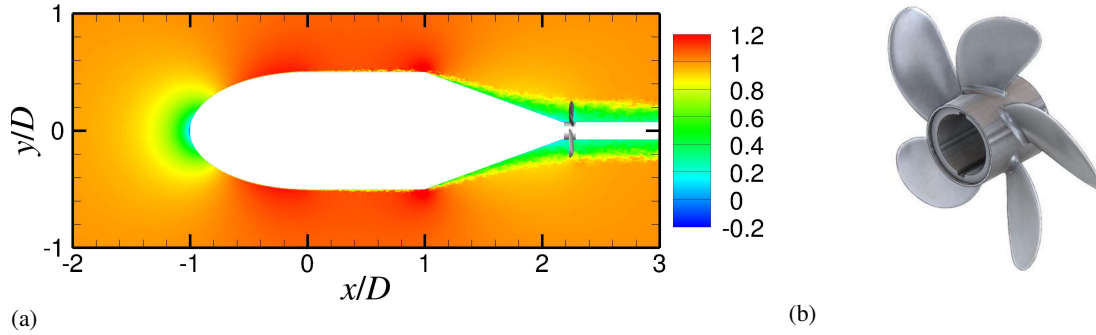


Figure 1: (a) Instantaneous axial velocity u_x/U_∞ in the x - y plane through the BOR axis; (b) rotor geometry.

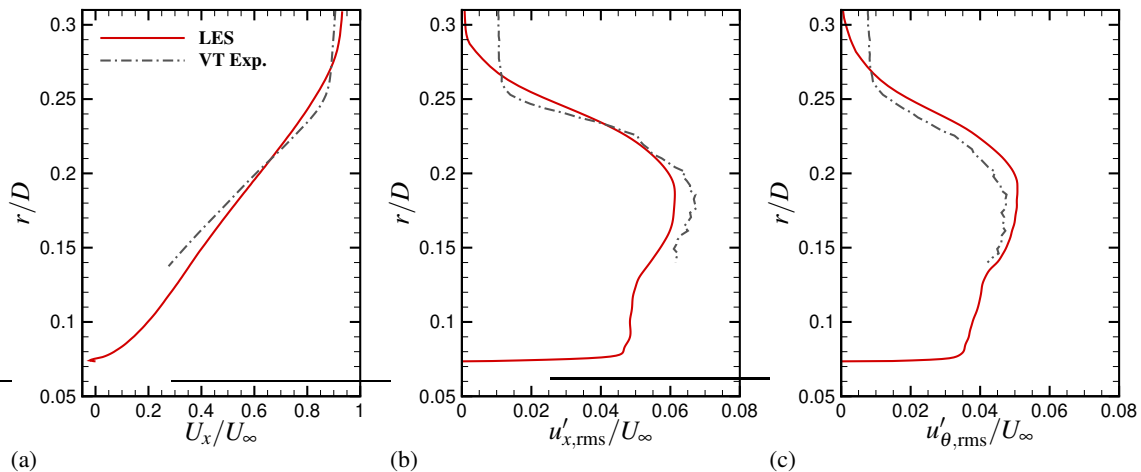


Figure 2: Velocity statistics at $x/D = 2.17$ compared with VT experimental data (Hickling, 2020; Balantrapu, 2021): (a) mean axial velocity; (b) axial turbulence intensity; (c) azimuthal turbulence intensity.

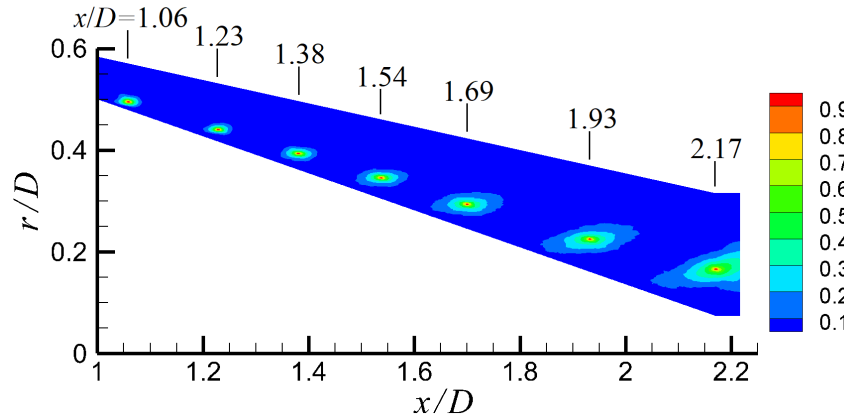


Figure 3: Two-point correlations of axial velocity fluctuations at seven locations along a mean streamline in the tail-cone TBL.

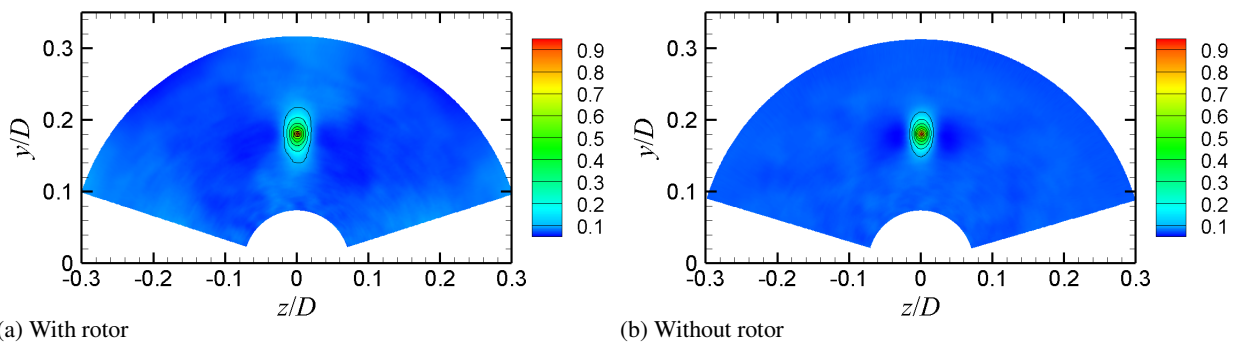


Figure 4: Two-point correlations of axial velocity fluctuations at $x/D = 2.17$, $r/D = 0.18$ in a cross-flow plane, with and without the rotor.

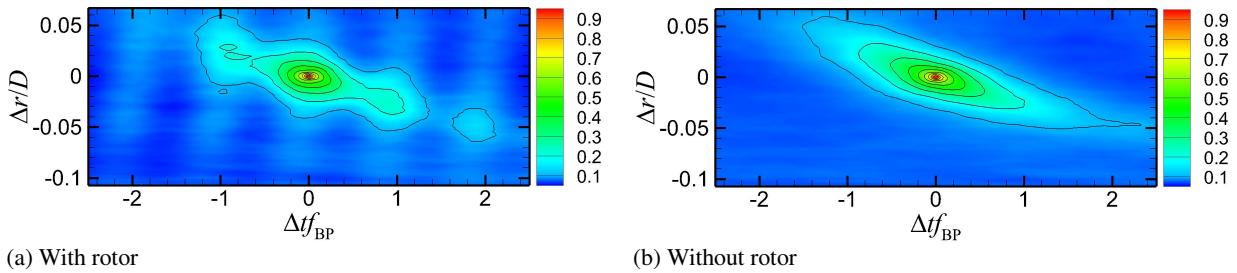


Figure 5: Radial space-time correlations of axial velocity fluctuations at $x/D = 2.17$, $r/D = 0.18$ with and without the rotor.

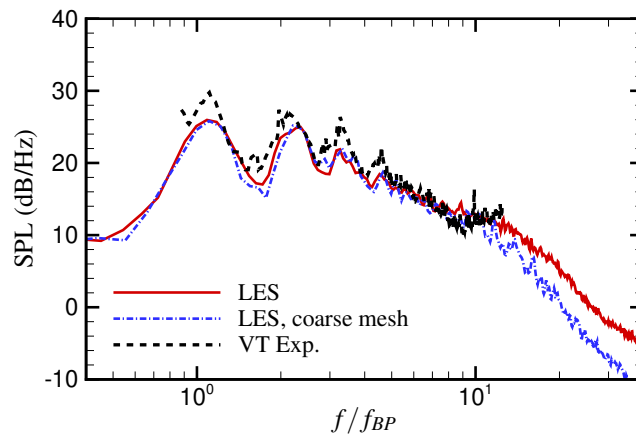


Figure 6: Computed sound pressure spectra compared with the microphone array measurement from the VT experiment (Hickling et al., 2019).

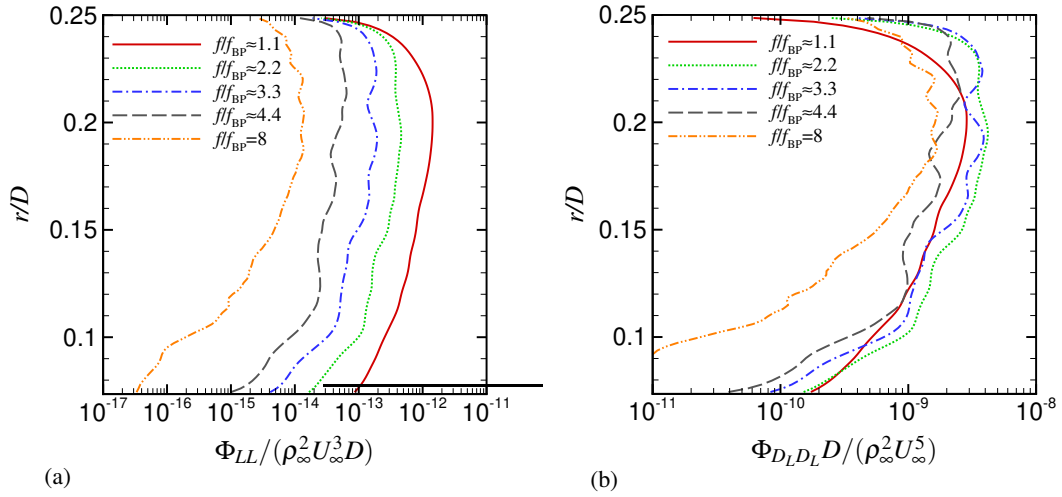


Figure 7: Radial distributions of the frequency spectra of (a) unsteady sectional force, and (b) sectional dipole source at five discrete frequencies.

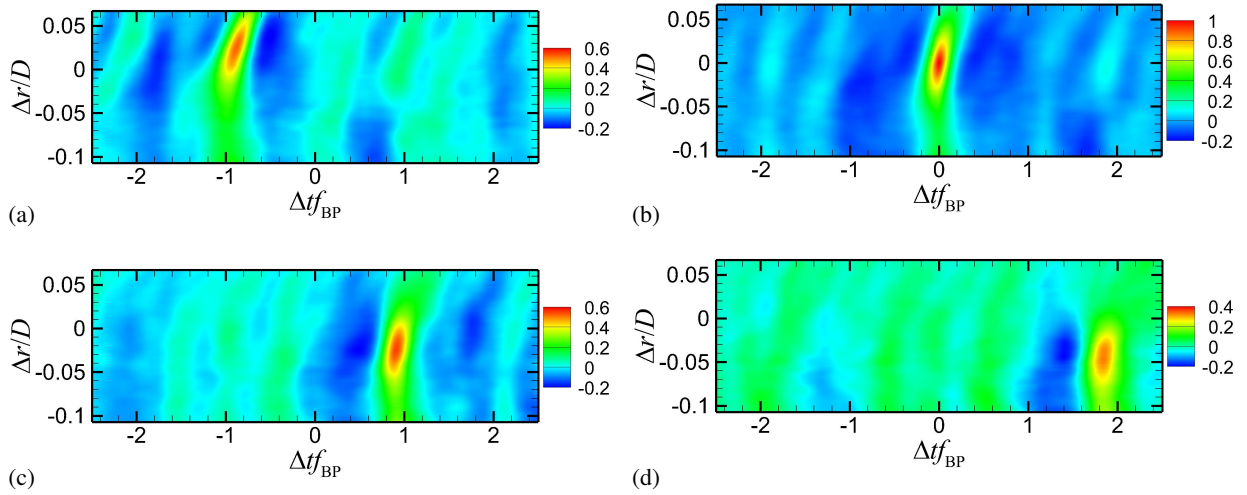


Figure 8: Space-time correlation coefficient of the unsteady sectional forces on blades m and n , $C_{LL}^{(m,n)}(r/D = 0.18, \Delta r, \Delta t)$: (a) $C_{LL}^{(1,5)}$; (b) $C_{LL}^{(1,1)}$; (c) $C_{LL}^{(1,2)}$; (d) $C_{LL}^{(1,3)}$.

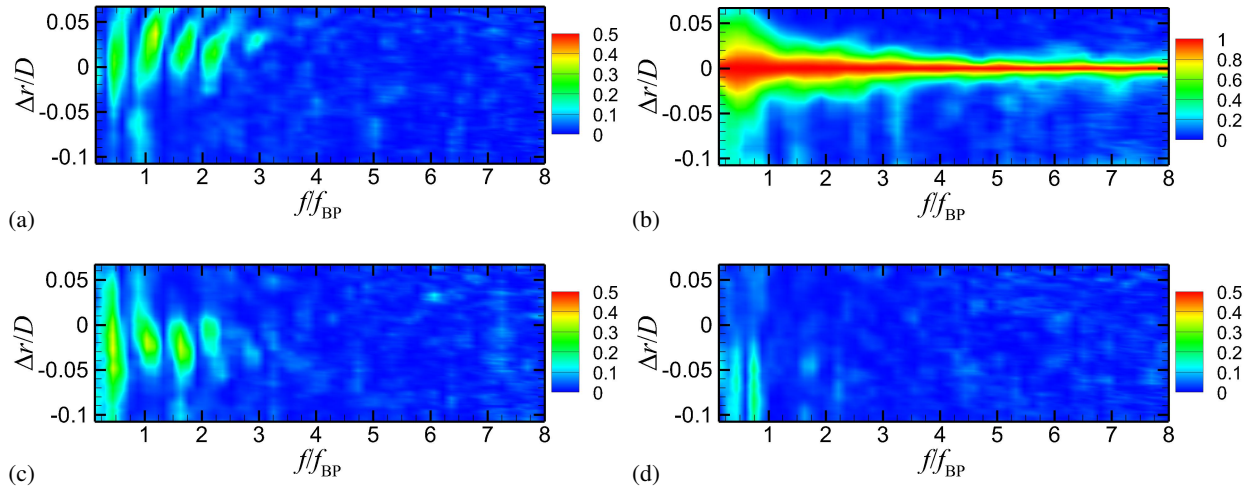


Figure 9: Coherence between the sectional dipole sources on blades m and n , $\gamma_{D_L D_L}^{2(m,n)}(r/D = 0.18, \Delta r, \Delta t)$: (a) $\gamma_{D_L D_L}^{2(1,5)}$; (b) $\gamma_{D_L D_L}^{2(1,1)}$; (c) $\gamma_{D_L D_L}^{2(1,2)}$; (d) $\gamma_{D_L D_L}^{2(1,3)}$.